# Outstanding Performance of Highly-Dispersed Zinc Species on Zeolites for the Continuous and Selective Dehydrogenation of Ethane with $CO_2$ as Soft Oxidant

*Jiaxu Liu,*[a] Ning He,[a] Zhenmei Zhang,[a] Jinpeng Yang,[a,b] Xiao Jiang,*[c] Ji Su,*[d] Miao Shu,[e] Rui Si,*[e] Guang Xiong,[a] Hongbin Xie,*[b] and Gianvito Vilé*[f]*

[a] State Key Laboratory of Fine Chemicals & Department of Catalytic Chemistry and Engineering, Dalian University of Technology, 116024 Dalian (China).

[b] Key Laboratory of Industrial Ecology and Environmental Engineering, Department of Environmental Science and Technology, Dalian University of Technology, 116012 Dalian (China).

[c] Chemical Science Division, Oak Ridge National Laboratory, 1 Bethel Valley Rd, 37830 Oak Ridge, Tennessee (United States).

[d] Materials Sciences Division, Molecular Foundry, Material Science Division, Lawrence Berkeley National Laboratory, 94720 Berkeley, California (United States).

[e] Shanghai Synchrotron Radiation Facility, Shanghai Institute of Applied Physics, Chinese Academy of Sciences, 201204 Shanghai (China).

[f] Department of Chemistry, Materials, and Chemical Engineering "Giulio Natta", Politecnico di Milano, Piazza Leonardo da Vinci 32, 20133 Milano (Italy).

[*] Corresponding authors. E-mails: liujiaxu@dlut.edu.cn, jiangx@ornl.gov, jisu@lbl.gov, sirui@sinap.ac.cn, hbxie@dlut.edu.cn, and gianvito.vile@polimi.it.

ABSTRACT

We report herein the preparation, characterization, and outstanding catalytic performance of a series of heterogeneous catalysts featuring highly-dispersed zinc sites on zeolitic SSZ-13 and ZSM-5 frameworks. The materials were evaluated in the oxidative dehydrogenation of ethane with $CO_2$ as a soft oxidant, a very important reaction for the synthesis of platform chemicals. In particular, we found that $Zn_{2.92}$/NaS50 exhibits high ethane conversion ability, excellent $CO_2$ transformation ability, and good selectivity. In line with the experimental results, we show that the highly-selective character is due to the characteristic compositional structure of the zeolite support and its topology that can effectively confine $CO_2$. An in-depth molecular analysis via operando studies and DFT calculation showed that the rate-limiting step of reaction with $CO_2$ was the second C-H bond dissociation to give ethene. The addition of $CO_2$ effectively reduced the energy barrier of this step, favoring desorption and limiting byproduct formation. Overall, this work demonstrates the breakthrough potential of novel heterogeneous catalysts made of highly-dispersed zinc species on zeolites in relevant transformations.

KEYWORDS. Reforming; Oxidative Dehydrogenation; $CO_2$ conversion; Zeolites; Single-Site Catalysis.

## 1. Introduction

As the economy and world population continue to rise, $CO_2$ emissions have reached 33.3 billion tons in 2019 [1]. Thus, a large number of endeavors are increasingly been paid to technologies that can capture, store, and/or utilize carbon dioxide, a gas that tends to accumulate in the atmosphere and is among the responsibles for the 'greenhouse effect' [2-9]. Among those, methods that can catalytically convert $CO_2$ into value-added molecules are particularly interesting, since such methods will create an opportunity to convert a waste into a commodity while preventing it from entering the atmosphere [10,11].

Catalytic hydrogenation of $CO_2$ into methanol [12,13], formate [14-16], and other valuable chemicals [17-19] is often considered a promising approach for the direct utilization of this small molecule. However, the transportation, use, and storage of gaseous $H_2$ is associated with safety issues and multiple logistic challenges [20]. Searching for alternative and cost-effective routes that utilize $CO_2$ is crucial for the realization of a catalytic and circular waste-to-product platform.

Oxidative dehydrogenation of ethane (ODE) is an energy-efficient and environmentally-promising approach to convert ethane into ethylene, which is a major feedstock for the synthesis of a wide variety of commercial products such as polyethylene, ethylene oxide, ethylene glycol, and styrene [21-28]. Ethane is the second largest component of shale gas and has high molar content of hydrogen (75%), which is second only to methane (80%). More importantly, the C-H bond of ethane is easier to break than that of methane [27], making it an alternative hydrogen source and a useful starting point for sustainable C-H activation in the absence of $H_2$. However, the direct ODE is thermodynamically limited and is highly endothermic ($\Delta H°_{298} = +136.5$ kJ mol$^{-1}$), requiring extremely high temperatures (>900°C). To overcome the excessive energy consumption of such process, $CO_2$ has been recently proposed as a soft oxidant to alter the dehydrogenation pathway, based on the reaction $C_2H_6 + CO_2 \rightarrow C_2H_4 + CO + H_2O$ [22-25]. This would reduce the operating temperature to milder conditions (400-600°C) [25,26]. Besides, owing to the presence of $CO_2$, the equilibrium conversion of ethane would be shifted to the product and this can also reduce the amount of coke formed on the catalysts at elevated temperature, via the reverse Boudouard reaction

($CO_2 + C \rightarrow 2CO$), increasing the stability of the catalysts. Thus, the strategy to co-convert ethane and $CO_2$ is feasible and can supply valuable chemicals while mitigating detrimental $CO_2$ emissions.

Up to now, heterogeneous catalysts featuring metal-based particles of Ga, Fe, Ni, Pt, Co, and V, deposited on a variety of supports, such as ZSM-5, $SiO_2$, $Al_2O_3$, $TiO_2$, SBA-15, MSU-x, MCM-41, clinoptilolite, and SAPO-34, have been reported for the oxidative dehydrogenation of ethane using $CO_2$ as mild oxidant ($CO_2$-ODE) [21-28]. Unfortunately, these catalysts have only shown common unsatisfactory shortcomings, such as relatively low $CO_2$ conversion at similar $C_2H_6$ conversion. For example, in the case of Cr/NaZ50, the $CO_2$ utilization rate is relatively low, considering the $C_2H_6$ conversion of 65% and the $CO_2$ conversion of only 22% at 650°C [30]. On the contrary, it is expected that the prepared catalysts have high ethane and $CO_2$ transformation ability, and exhibit good thermal stability.

SSZ-13, an aluminosilicate zeolite possessing CHA cages connected by 8-membered ring with a small pore opening of 3.8 Å, was firstly patented by Chevron in 1985 [31]. In recent years, Cu-exchanged SSZ-13 has been commercialized in the selective catalytic reduction of $NO_x$ from diesel engine exhaust treatment [32,33]. One of the significant advantages of SSZ-13 is its excellent hydrothermal stability, enabling diesel exhaust temperature rise well above 800°C [34]. More importantly, Hudson *et al*. [35] found that, owing to its special pore structure, SSZ-13 exhibited unconventional, highly selective $CO_2$ adsorption ability, indicating that the small pore of SSZ-13 can effectively confine $CO_2$ in the channel, which is expected to be beneficial for the conversion of $CO_2$. Based on above discussion, we believed that SSZ-13 may have been the ideal choice as catalyst support for the $CO_2$-ODE.

In this work, we report the preparation, characterization, and excellent catalytic performance of a series of SSZ-13 zeolitic catalysts containing isolated Zn species in its framework. The choice of Zn is justified by the fact that, for the conversion of light alkanes, Zn-modified zeolites have shown high efficiency for the dehydrogenation of short-chain hydrocarbons at relatively low temperature [36-38]. The catalytic performance was compared with Zn-modified zeolites having different topologies, such as Zn/ZSM-5.

Based on the experimental results, we found that the Zn/SSZ-13 catalysts exhibit ultra-high $CO_2$ and $C_2H_6$ conversion, and the $CO_2$ and $C_2H_6$ conversion was almost at the equivalent level. This made a sharp contrast to Zn/ZSM-5 catalyst, showing only low $CO_2$ conversion. The catalytic performance was further rationalized via Density Functional Theory calculations and *operando* studies, to unlock for the very first-time structure-performance relationships of these novel single-site zeolitic catalysts.

## 2. Experimental

**Catalyst preparation.** Na/SSZ-13 and Na/ZSM-5 zeolites with a total $SiO_2/Al_2O_3$ ratio of 50 and crystal size of approximately 1 μm were purchased from Dalian Ligong Qiwangda Chemical Technology (DQ-TECH). The Na/MCM-22 and Na/Y zeolites were commercially produced by DQ-TECH and Nankai Catalyst Company, respectively. The Zn-containing samples were obtained by incipient wet impregnation. The impregnation was conducted at 80°C for 1 h by using an aqueous solution of zinc nitrate with different Zn concentration (1, 3, 5 and 9 wt.%). The amount of aqueous solution to be used was chosen based on the Zn loading that was expected in the materials. After impregnation, the samples were dried at 110°C for 12 h and then calcined at 540°C in a controlled environment, using flowing dry air for 6 h.

**Catalyst characterization.** The real loadings of Zn in the modified samples were determined by X-ray fluorescence (XRF) on a Bruker SRS3400 spectrometer. X-ray diffraction (XRD) patterns were obtained on a Rigaku D-max-2004 diffractometer using Cu Kα radiation (40 kV, 100 mA) and 0.02° $min^{-1}$ $2\theta$ scanning speed. Temperature-programmed desorption of $CO_2$ ($CO_2$-TPD) was employed to investigate the overall basicity of the catalysts. The profiles were collected with a Quantachrome ChemBet 3000 chemisorb instrument. The samples (150 mg, 380-830 μm sieve fraction) were pretreated in He (99 wt% purity, Dalian Special Gases Ltd.) at 600°C for 1 h and then cooled down to 100°C for $CO_2$ adsorption. $CO_2$ (99 wt% purity, Dalian Special Gases Ltd.) adsorption was carried out at 100°C for 30 min with a mixture of 5% $CO_2$ in He. After adsorption the cell was purged for 30 min in 50 mL $min^{-1}$ He flow to

remove eventual non-chemically adsorbed $CO_2$ species. Then, $CO_2$-TPD profiles were recorded in a 50 mL $min^{-1}$ He flow by ramping the temperature from 100 to 600°C at a rate of about 16°C $min^{-1}$. The effluent was analyzed by a quadrupole mass spectrometer (Omnistar, 1-200 amu, QMS 200). The cokes on the used catalysts were measured by a thermogravimetric analyzer (TGA/DSC 1/1100, Mettler Toledo). For textural data, nitrogen physisorption was conducted on a Micromeritics ASAP 3020 instrument at -196°C. Prior to the measurement, the samples (380-830 μm sieve fraction) were degassed at 400°C for 6 h. The surface area was calculated by Brunauer-Emmett-Teller (BET) method using the adsorption branch in the $p/p_o$ range from 0.01 to 0.12 [39]. The pore volumes were estimated at $p/p_o$ of 0.99, while the micro- and mesoporosity were discriminated by *t*-plot method [40,41]. *Operando* Fourier transform infrared (FTIR) spectrometer was employed to study the conversion of $CO_2$ and ethane (99 wt.% purity, Dalian Special Gases Llt.) over pristine and Zn-modified NaS50 catalysts at 300°C and atmospheric pressure. The catalysts were pressed into self-supporting thin wafers (1 $cm^2$); these were placed in the infrared reactor cell and activated at 400°C for 4 h under vacuum ($10^{-3}$ Pa). The spectra were then recorded at a resolution of 4 $cm^{-1}$ with 64 scans in the region of 4000-1000 $cm^{-1}$. The intensities of the reference and sample beams were adjusted to the same level. The effluent from IR reactor cell was analyzed by a quadrupole mass spectrometer (Omnistar, 1-200 amu, QMS 200). The X-ray absorption fine structure (XAFS) spectra at Zn K ($E_0$ = 9659 eV) edge was performed at BL14W1 beamline of Shanghai Synchrotron Radiation Facility (SSRF) operated at 3.5 GeV under 'top-up' mode, and using a constant current of 240 mA. The XAFS data were recorded under fluorescence mode with a Lytle ion chamber. The energy was calibrated accordingly to the absorption edge of pure Zn foil. Athena and Artemis codes were used to extract the data and fit the profiles. For the X-ray absorption near edge structure (XANES) part, the experimental absorption coefficients as function of energies $\mu(E)$ were processed by background subtraction and normalization procedures, and reported as 'normalized absorption' with $E_0$ = 9659 eV for all the investigated samples and Zn foil/ZnO standard. For the extended X-ray absorption fine structure (EXAFS) part, the Fourier transform (FT) data in the *R* space were analyzed by applying ZnO, metallic Zn and first-shell approximate model for Zn-O, Zn-Zn and Zn-Al contributions.. The passive electron factors, $S_0^2$, were determined by fitting the

experimental data on Ni foils and fixing the coordination number (*CN*) of Zn-Zn to be 6 + 6, and then fixed for further analysis of the measured samples. The parameters describing the electronic properties (*e.g.*, correction to the photoelectron energy origin, $E_0$) and local structure environment including *CN*, bond distance (*R*) and Debye-Waller factor around the absorbing atoms were allowed to vary during the fit process. The fitted ranges for *k* and *R* spaces were selected to be *k* =3–12 $Å^{-1}$ with *R* = 1.1–4.0 Å ($k^3$ weighted).

**Catalyst performance.** A continuous-flow fixed-bed microreactor was used to evaluate the ethane and $CO_2$ co-conversion over both pristine and Zn modified NaS50 catalysts. All samples were crushed and sieved into 20-40 mesh particles before they were loaded into the reactor. In particular, 2.0 g of catalyst were loaded in the middle part of a stainless-steel reactor with 600 mm in length and 10 mm in diameter. The remaining parts was filled with ceramic balls with diameter of 10-20 mesh. The temperature of the catalyst bed was monitored by a thermal couple. Prior to the reaction, the catalyst was kept at 540°C for 1 h in $N_2$ flow (1 mL $min^{-1}$) to remove any adsorbed water. The flow of feedstock (5% ethane, 5% $CO_2$, and 90% helium) was controlled by mass spectrometer. The hydrocarbon products were analyzed with an FID detector while the hydrogen and CO were analyzed with a TCD detector.

**Computational method.** The calculated model with 48T was obtained by cutting the periodic CHA-type zeolite, as is shown in **Figure 1**. In all the models, the dangling bonds were saturated with hydrogen atoms pointing to the next lattice oxygen atom, and the Si-H bond length was set to 1.46 Å. The calculations were performed on Gaussian 09 program package [42]. To improve the energetic properties and consider the effect of the entire zeolite framework on the reaction mechanism, a two-layer scheme ONIOM model was employed [43]. The region in an intimate relationship to catalytic reactions was treated at high-level functional ωB97XD recently developed by Chai and Head-Gordon, along with the 6-31+G(d,p) basis set for accuracy, which is a long-range corrected functional [44]. In particular, ωB97XD is a long-range corrected hybrid density functional with damped atom-atom dispersion corrections and has been found more reliable for the calculation of the dispersion as well as charge transfer (CT) excited states than results

found using earlier density functionals. The regions away from the active center were treated at lower-level with the semi-empirical calculation method (UFF) for efficiency. For all calculations, the positions of the terminal $SiH_3$ atoms were fixed, whereas the positions of the remaining atoms and guest molecules were left for optimization. Many experimental and theoretical studies have indicated that the distribution of Al in framework of zeolite would influence the species of metal ions located on catalysts. Based on previous experimental data [45], there are two possible Zn species: zinc ion $Zn^{2+}$ and oxidic zinc ion $(Zn\text{-}O\text{-}Zn)^{2+}$. Therefore, all possible models with different location of Al and Zn species were considered. Models 6M_1 and 8M_1 with $Zn^{2+}$ and $(Zn\text{-}O\text{-}Zn)^{2+}$, respectively, are two the most preferential models from the view of thermodynamics. Thus, in this work, these two models were selected to investigate the reaction mechanism. The transition state structures were characterized by means of frequency calculations with only one imaginary frequency. The intrinsic reaction coordinate (IRC) method was used when necessary to identify the two minima connected by a transition state. To obtain accurate energies, single-point energy calculations in the optimized model were further refined at the theoretical level of ωB97XD/6-311++G(d, p).

## 3. Results and Discussion

### 3.1 Catalyst characterization

A variety of Zn/zeolite catalysts were prepared in this study. **Figure 2** shows the XRD patterns of the pure and Zn-modified NaS50 and NaZ50. In all cases, characteristic peaks assigned to the corresponding topological structures of the respective zeolites are present, and no peaks related to the Zn phases are observed. This indicates the high dispersion of Zn species in the samples. Such result is confirmed by our HRTEM micrographs (**Figure 3**) which show highly-dispersed zinc and no zinc particles. According to the nitrogen physisorption results (**Table 1**), the microporous surface area and microporous volume of the modified samples gradually decrease as the amount of Zn increases. This result is independent from the

topological zeolite structure, and is confirmed for the different NaS50, NaZ50, NaMCM, NaY, and NaSAPO samples. It is deduced that most of the Zn species over Zn/NaZ50 and Zn/NaS50 are located inside the channel of zeolite, thus affecting the (micro)pore volume of the materials. The $CO_2$ adsorption isotherms measured at 298 K and $CO_2$-TPD are shown in **Figures 4** and **5**, respectively. The two NaS50-based samples, with or without Zn, exhibit a much better $CO_2$ adsorption capacity, which indicates that the SSZ-13 framework can accommodate larger quantities of $CO_2$, in spite of its small pore opening. The total $CO_2$ adsorption over NaZ50 is instead very limited. Similarly, from the $CO_2$-TPD results, it appears that the Zn/NaS50 samples have a broad desorption peak around 100-150˚C, while for NaZ50 no desorption peak in the whole temperature range is observed. The characterization points to a better $CO_2$ adsorption ability of the NaS50-based materials, and no adsorption over the NaZ50 equivalent. **Figure 6** depicts the $NH_3$-TPD profiles of the zeolites, reveling information on the acidic strength of the materials. The NaS50 and NaZ50-based catalysts, in fact, have weak acid sites, as confirmed by the low temperature desorption peak around 100-300°C. A relatively small fraction of strong acid sites is present on the CHA framework. Since Lewis and Brønsted acid sites can be differentiated only by pyridine adsorption and FTIR spectroscopy, this is shown in **Figure 7**. In particular, the adsorption at 1621 $cm^{-1}$ over the Zn-containing NaS50 samples is assigned to pyridine molecules adsorbed on Lewis acid sites over these samples. Since these sites are absent on the pristine materials, we deduce that they are an effect on the incorporation of zinc species into the NaS50 structure.

### 3.2 Catalyst evaluation

The oxidative dehydrogenation of ethane with $CO_2$ as a soft oxidant has been investigated as a function of temperature over NaS50 and NaZ50 catalysts with different loadings of Zn (**Figure 8**). Compared with the parent zeolites without any incorporation of Zn species, which have negligible activity in the reaction, the addition of Zn significantly increases the $C_2H_6$ and $CO_2$ conversion. The conversion of both reactant can be linearly correlated with the Zn loading, indicating that Zn plays a catalytic role in this reaction. The

absence of any activity in the parent zeolite is a very distinctive character to discriminate between a doped and a single-site catalyst. In our case, since the bare zeolitic framework is inactive, we can confidently state that the Zn-containing materials function as 'single-site catalysts', and that it is the presence of highly-dispersed metal sites that contributes to the observed activity. Specifically, $Zn_{2.92}$/NaS50 stands out as the most active catalyst. In fact, at 650°C, the $CO_2$ and $C_2H_6$ conversion over $Zn_{2.92}$/NaS50 are *ca.* 60% and 70%, respectively. The trend is confirmed for the NaZ50-based catalysts, with the most loaded Zn catalyst displaying a $CO_2$ and a $C_2H_6$ conversion of *ca*. 20% and 50%, respectively. From this data, it can be observed that Zn-containing NaS50 catalysts are slightly more active than the corresponding NaZ50-based materials in the $CO_2$-ODE. This aspect (and the important role of the framework) will be discussed in great depth in the following paragraphs.

**Figure 9** shows the correlation between the degrees of conversion of ethane and $CO_2$ for Zn/NaS50 and Zn/NaZ50. For the case of $Zn_{2.92}$/NaS50, the ratio between the conversion of $CO_2$ and that of ethane is around 0.86, which is close to the ideal value (*i.e.*, 1), representing an equivalent co-conversion of $CO_2$ and ethane. In such situation, we expect the catalyst to be highly selective since both reactants interact based on the reaction stoichiometry $C_2H_6 + CO_2 \rightarrow C_2H_4 + CO + H_2O$ [22-25]. Instead, for Zn/NaZ50, the conversion of $C_2H_6$ is at least two times higher than that of $CO_2$. This points to potential side reactions, which are inevitable depending on the zeolitic framework and include steam reforming of ethane to generate methane, hydrogenolysis, and coking. In practice, the most common method to solve this problem is by increase the feedstock of $CO_2$ to suppress any side reaction, which may result in slightly higher product selectivities but low conversions of $CO_2$ and increased separation costs (as shown in **Figure 10**).

To discuss about product selectivities, it is critical to compare catalysts at a similar degree of conversion. This has been done in **Figure 11**, where four selected catalysts are compared at a $CO_2$ conversion of 10%. It appears that all catalysts have outstanding $C_2H_4$ selectivities well-above 90%. The complete ethene selectivity patterns observed over the different Zn-containing NaS50 and NaZ50 catalysts at various temperatures confirm this trend and are depicted in **Figure S1** in the Supporting Information.

### 3.3 Importance of the zeolite topological structure

It is well known that, in zeolite catalysis, the material performance is strongly dependent on the compositional and topological structure of the parent zeolite [38,39]. Hence, a series of Zn-containing zeolite catalysts have been prepared and their activities was compared with the excellent performance of $Zn_{2.90}$/NaS50 (**Figure S2**). In particular, the activity (normalized to the amount of Zn loading) is different depending on the chosen zeolite framework, and goes in the sequence NaS50 > NaZ50 > MCM-22 > NaY. This is opposite with that of the zeolite pore diameter (SSZ-13 (0.38 Å) < ZSM-5 and MCM-22 (0.55 Å) < Y(0.78 Å)), pointing to the fact that zeolites with small pore openings are preferable due to a potential more controlled diffusion and adsorption of $CO_2$.

Finally, the catalytic performance of Zn/NaS50 was evaluated as a function of time-on-stream (**Figure S3**). The illustration, in particular, depicts the conversion and selectivity obtained over $Zn_{0.89}$/NaS50 and $Zn_{2.92}$/NaS50. The two catalysts are chosen to evaluate time-on-stream behaviors over 200 min of reaction, because of their low and high metal loading. For $Zn_{0.89}$/NaS50, a stable catalytic performance is observed, since the $C_2H_6$ conversion and $C_2H_4$ selectivity remain constant at *ca*. 30% and around 95-98%, respectively. Instead, for $Zn_{2.92}$/NaS50, the activity slightly decreases initially as the time-on-stream increases. We can deduce that lower Zn loading gives a more stable behavior while, at high Zn amount, the there is a partial decrease of catalytic activity. Through the thermogravimetric analysis of the weight loss of the spent catalyst, it was found that this deactivation is mainly caused by carbon deposits (which instead are not detected over $Zn_{0.89}$/NaS50).

### 3.4 Molecular-level understanding via DFT and operando studies

To rationalize at a molecular level the catalytic results and also understand how $CO_2$ helps the dehydrogenation of $C_2H_6$, advanced spectroscopic characterizations and DFT calculations have been performed to comparatively study, with and without $CO_2$, the energy surfaces of the Zn-based single site catalysts in the dehydrogenation of $C_2H_6$. In particular, based on EXAFS data (**Figure S4** and **Table S1**),

two calculated models, $(Zn\text{-}O\text{-}Zn)^{2+}$ and $Zn^{2+}$, which respectively represent zinc oxide and zinc ion located on SSZ-13 zeolites, have been used to investigate the dehydrogenation mechanism of ethane and the role of $CO_2$ in the reaction. DFT shows that after a physical adsorption, ethane dissociates via C-H bond break and is adsorbed on the active sites. Ethyl intermediates and hydroxyl groups (Si(OH)Al for $Zn^{2+}$ model, ZnOH for $(Zn\text{-}O\text{-}Zn)^{2+}$ model) are formed. Then, ethyl intermediates go through the second C-H bond break to desorb ethene and leave Zn-H on the surface of catalysts. Subsequently, the desorption of $H_2$ occurs in the absence of $CO_2$. As shown in **Figure 12**, the energy profiles for the two models are comparable. Also, the desorption of $H_2$ is the most energy demanding step, requiring about 38.57 kcal/mol and 35.73 kcal/mol on $Zn^{2+}$ and $(Zn\text{-}O\text{-}Zn)^{2+}$, respectively. Interestingly, the existence of $CO_2$ effectively reduces the energy barriers required for the surface hydrogen removal. In fact, the addition of $CO_2$ on the $[Zn\text{-}H^-]^+$ moiety generates $[Zn\text{-}COOH]^+$, which only need to overcome a barrier of 26.13 kcal/mol for $Zn^{2+}$ and of 13.81 kcal/mol for $(Zn\text{-}O\text{-}Zn)^{2+}$.

To verify the reliability of calculated reaction mechanism, *operando* dual-beam Fourier transform infrared spectrometry (DB-FTIR) was performed, to provide a clear picture of the dynamic surface processes involved in gas/solid heterogeneous catalysis under real reaction conditions, and eventually observe directly the reaction process of $C_2H_6$ with and without $CO_2$ over $Zn_{2.92}$/NaS50 at 300°C. As shown in **Figure 13**, the IR peaks at 3730 $cm^{-1}$, 3602 $cm^{-1}$, and 3571 $cm^{-1}$, which can be ascribed to O-H stretching vibrations, and the peaks at 2800-3000 $cm^{-1}$, which are attributed to the C-H stretching vibrations, are similar for two reaction conditions. It indicates that the mechanisms of catalytic oxidative dehydrogenation of ethane are similar, independently from the presence of $CO_2$. However, a characteristic stretching vibration in the region 2385-2296 $cm^{-1}$, typically assigned to $HCOO^-$, is only observed for the reaction with $CO_2$ as soft oxidant, and methane acid as intermediate product was also detected in the effluent of DB-FTIR by mass spectroscopy (**Figure 14**).

The scheme of the overall reaction mechanism for the oxidative dehydrogenation of ethane in the presence of $CO_2$ is depicted in **Figure S5**. The major difference with a standard ethane dehydrogenation

without $CO_2$, is the second C-H bond dissociation to desorb ethene, which is in that case the rate-limiting step for dehydrogenation of ethane with $CO_2$. The addition of $CO_2$ effectively reduces the energy barrier of the surface hydrogen removal, which is favorable to the removal of surface hydrogen to avoid hydrogenolysis to the byproduct methane. In addition, it is worth mentioning that the energy barrier of surface hydrogen removal for $(Zn\text{-}O\text{-}Zn)^{2+}$ is decreased more (about 21.92 kcal/mol) than that of $Zn^{2+}$ (about 12.44 kcal/mol).

## 4. Conclusion

In this study, we have investigated the $CO_2$-mediated oxidative dehydrogenation of $C_2H_6$ over a new family of heterogeneous catalysts made of highly-dispersed Zn species entrapped in a zeolite carrier. It was found that $Zn_{2.92}$/NaS50 exhibits excellent catalytic performance for the conversion of $C_2H_6$, at a $CO_2/C_2H_6$ conversion ratio close to the ideal case of 1. Compared to Zn-based catalysts made using other zeolites, Zn/NaS50 stands out as a very active and selective material, owing to its unique channel structure that can effectively confine $CO_2$ in the channel, increasing the conversion of $CO_2$ and suppressing any side reaction. The Zn-containing NaS50 catalysts also exhibit good hydrothermal stability. Based on DFT calculations, it has been found that the reasons for this outstanding behavior can be correlated with the rate-limiting step for the dehydrogenation of ethane with $CO_2$, which is the second C-H bond dissociation to desorb ethene. The addition of $CO_2$ effectively reduces the energy barrier of the surface hydrogen removal, which is favorable to the removal of surface hydrogen in time and avoids hydrogenolysis to produce methane. Overall, this work reports not only a novel family of single-site catalysts based on zeolites, but also demonstrates a promising approach to efficient convert $CO_2$ and $C_2H_6$ by using Zn-containing NaS50 as effective catalysts.

ASSOCIATED CONTENT

**Supporting Information**. Additional characterization data of the materials.

## AUTHOR INFORMATION

### Corresponding Authors

liujiaxu@dlut.edu.cn (Prof. Jiaxu Liu, Dalian University of Technology)

jiangx@ornl.gov (Dr. Jiang Xiao, Oak Ridge National Laboratory)

jisu@lbl.gov (Dr. Ji Su, Lawrence Berkeley National Laboratory)

sirui@sinap.ac.cn (Prof. Rui Si, Shanghai Institute of Applied Physics)

hbxie@dlut.edu.cn (Prof. Hongbin Xie, Dalian University of Technology)

gianvito.vile@polimi.it (Dr. Gianvito Vilé, Politcnico di Milano)

### Author Contributions

The manuscript was written through contributions of all authors. All authors have given approval to the final version of the manuscript.

### Funding Sources

G.V. thanks Fondazione Bracco and Fondazione Politecnico di Milano for funding.

## REFERENCES

[1] International Energy Agency, Global $CO_2$ emissions in 2019. https://www.iea.org/articles/global-co2-emissions-in-2019 (accessed in October **2020**).

[2] E. S. Sanz-Pérez, C. R. Murdock, S. A. Didas, C. W. Jones, Direct capture of $CO_2$ from ambient air. *Chem. Rev.* **2016**, *116*, 11840-11876.

[3] S.-Y. Lee, S.-J. Park, A review on solid adsorbents for carbon dioxide capture. *J. Ind. Eng. Chem.* **2015**, *23*, 1-11.

[4] M. Bui, C. S. Adjiman, A. Bardow, E. J. Anthony, A. Boston, S. Brown, P. S. Fennell, S. Fuss, A. Galindo, L. A. Hackett, J. P. Hallett, H. J. Herzog, G. Jackson, J. Kemper, S. Krevor, G. C. Maitland, M. Matuszewski, I. S. Metcalfe, C. Petit, G. Puxty, J. Reimer, D. M. Reiner, E. S. Rubin, S. A. Scott, N. Shah, B. Smit, J. P. Martin Trusler, P. Webley, J. Wilcox, N. M. Dowell, Carbon capture and storage (CCS): the way forward. *Energy Environ. Sci.* **2018**, *11*, 1062.

[5] C. Vogt, E. Groeneveld, G. Kamsma, M. Nachtegaal, L. Lu, C. J. Kiely, P. H. Berben, F. Meirer, B. M. Weckhuysen, Unravelling structure sensitivity in $CO_2$ hydrogenation over nickel. *Nat. Catal*. **2018**, *1*, 127-134.

[6] S. D. Kenarsari, D. Yang, G. Jiang, S. Zhang, J. Wang, A. G. Russell, Q. Wei, M. Fan, Review of recent advances in carbon dioxide separation and capture. *RSC Adv*. **2013**, *3*, 22739-22773.

[7] K. Li, B. Peng, T. Peng, Recent advances in heterogeneous photocatalytic $CO_2$ conversion to solar fuels. *ACS Catal*. **2016**, *6*, 7485-7527.

[8] P. Gao, S. Dang, S. Li, X. Bu, Z. Liu, M. Qiu, C. Yang, H. Wang, L. Zhong, Y. Han, Q. Liu, W. Wei, Y. Sun, Direct production of lower olefins from $CO_2$ conversion via bifunctional catalysis. *ACS Catal*. **2018**, *8*, 571-578.

[9] R. Sen, A. Goeppert, S. Kar, G. K. Surya Prakash, Hydroxide based integrated $CO_2$ capture from air and conversion to methanol. *J. Am. Chem. Soc.* **2020**, *142*, 4544-4549.

[10] P. Gao, S. Li, X. Bu, S. Dang, Z. Liu, H. Wang, L. Zhong, M. Qiu, C. Yang, J. Cai, W. Wei, Y. Sun, Direct conversion of $CO_2$ into liquid fuels with high selectivity over a bifunctional catalyst. *Nat. Chem.* **2017**, *9*, 1019-1024.

[11] M. Aresta, A. Dibenedetto, A. Angelini, Catalysis for the valorization of exhaust carbon: from $CO_2$ to chemicals, materials, and fuels. Technological use of $CO_2$. *Chem. Rev.* **2014**, *114*, 1709-1742.

[12] J. Graciani, K. Mudiyanselage, F. Xu, A. E. Baber, J. Evans, S. D. Senanayake, D. J. Stacchiola, P. Liu, J. Hrbek, J. Fernández Sanz, J. A. Rodriguez, Highly active copper-ceria and copper-ceria-titania catalysts for methanol synthesis from $CO_2$. *Science* **2014**, *345*, 546-550.

[13] F. Studt, I. Sharafutdinov, F. Abild-Pedersen, C. F. Elkjær, J. S. Hummelshøj, S. Dahl, I. Chorkendorff, J. K. Nørskov, Discovery of a Ni-Ga catalyst for carbon dioxide reduction to methanol. *Nat. Chem.* **2014**, *6*, 320-324.

[14] D. Preti, C. Resta, S. Squarcialupi, G. Fachinetti, Carbon dioxide hydrogenation to formic acid by using a heterogeneous gold catalyst. *Angew. Chem. Int. Ed*. **2011**, *50*, 12551-12554.

[15] S. Moret, P. J. Dyson, G. Laurenczy, Direct synthesis of formic acid from carbon dioxide by hydrogenation in acidic media. *Nat. Commun*. **2014**, *5*, 4017.

[16] S. Zhang, P. Kang, T. J. Meyer, Nanostructured tin catalysts for selective electrochemical reduction of carbon dioxide to formate. *J. Am. Chem. Soc*. **2014**, *136*, 1734-1737.

[17] M. B. Ansari, B.-H. Min, Y.-H. Mo, S.-E. Park, $CO_2$ activation and promotional effect in the oxidation of cyclic olefins over mesoporous carbon nitrides. *Green Chem*. **2011**, *13*, 1416-1421.

[18] M. Aresta, Carbon Dioxide as Chemical Feedstock, Wiley-VCH: New York, **2010**.

[19] S. Gao, Y. Lin, X. Jiao, Y. Sun, Q. Luo, W. Zhang, D. Li, J. Yang, Y. Xie, Partially oxidized atomic cobalt layers for carbon dioxide electroreduction to liquid fuel. *Nature* **2016**, *529*, 68-71.

[20] Y. S. H. Najjar, Hydrogen safety: the roadmap toward green technology. *Int. J. Hydrog. Energy* **2013**, *38*, 10716-10728.

[21] F. Rahmani, M. Haghighi, B. Mohammadkhani, Enhanced dispersion of Cr nanoparticles over nanostructured $ZrO_2$-doped ZSM-5 used in $CO_2$-oxydehydrogenation of ethane. *Microporous Mesoporous Mat.* **2017**, *242*, 34-49.

[22] M. D. Porosoff, M. N. Z. Myint, S. Kattel, Z. Xie, E. Gomez, P. Liu, J. G. Chen, Identifying different types of catalysts for $CO_2$ reduction by ethane through dry reforming and oxidative dehydrogenation. *Angew. Chem. Int. Ed.* **2015**, *54*, 15501-15505.

[23] R. Koirala, R. Buechel, S. E. Pratsinis, A. Baiker, Silica is preferred over various single and mixed oxides as support for $CO_2$-assisted cobalt-catalyzed oxidative dehydrogenation of ethane. *Appl. Catal. A* **2016**, *527*, 96-108.

[24] P. Taghavinezhad, M. Haghighi, R. Alizadeh, Sonosynthesis of $VO_x$/MCM-41 nanocatalyst enhanced by various metal oxides (Mg, AL, Zr) for $CO_2$-oxidative dehydrogenation of ethane to ethylene. *Microporous Mesoporous Mat.* **2018**, *261*, 63-78.

[25] Y. Cheng, T. Lei, C. Miao, W. Hua, Y. Yue, Z. Gao, Single-site $CrO_x$ moieties on silicalite: highly active and stable for ethane dehydrogenation with $CO_2$. *Catal. Lett.* **2018**, *148*, 1375-1382.

[26] R. Koirala, R. Buechel, F. Krumeich, S. E. Pratsinis, A. Baiker, Oxidative dehydrogenation of ethane with $CO_2$ over flame-made Ga-loaded $TiO_2$. *ACS Catal.* **2015**, *5*, 690-702.

[27] C. Baroi, A. M. Gaffney, R. Fushimi, Process economics and safety considerations for the oxidative dehydrogenation of ethane using the M1 catalyst. *Catal. Today* **2017**, *298*, 138-144.

[28] L. Lisi, L. Marchese, H. O. Pastore, A. Frache, G. Ruoppolo, G. Russo, Evaluating the catalytic performances of SAPO-34 catalysts for the oxidative dehydrogenation of ethane. *Top. Catal*. **2003**, *22*, 95-99.

[29] S. Yao, B. Yan, Z. Jiang, Z. Liu, Q. Wu, J. Lee, J. G. Chen, Combining $CO_2$ reduction with ethane oxidative dehydrogenation by oxygen-modification of molybdenum carbide. *ACS Catal.* **2018**, *8*, 5374-5381.

[30] Y. Cheng, C. Miao, W. Hua, Y. Yue, Z. Gao, Cr/ZSM-5 for ethane dehydrogenation: Enhanced catalytic activity through surface silanol. *Appl. Catal. A* **2017**, *532*, 111-119.

[31] S. I. Zones, Zeolite SSZ-13 and its method of preparation. US Patent n° 4544538, **1985**.

[32] A. M. Beale, F. Gao, I. Lezcano-Gonzalez, C. H. F. Peden, J. Szanyi, Recent advances in automotive catalysis for $NO_x$ emission control by small-pore microporous materials. *Chem. Soc. Rev.* **2015**, *44*, 7371-7405.

[33] C. Paolucci, I. Khurana, A. A. Parekh, S. Li, A. J. Shih, H. Li, J. R. Di Iorio, J. D. Albarracin-Caballero, A. Yezerets, J. T. Miller, W. N. Delgass, F. H. Ribeiro, W. F. Schneider, R. Gounder, Consequences

of exchange-site heterogeneity and dynamics on the UV-visible spectrum of Cu-exchanged SSZ-13, *Chem. Sci.* **2017**, *357*, 898-903.

[34] Y. J. Kim, J. K. Lee, K. M. Min, S. B. Hong, I.-S. Nam, B. K. Cho, Hydrothermal stability of Cu-SSZ13 for reducing $NO_x$ by $NH_3$. *Journal of Catalysis* **2014**, *311*, 447-457.

[35] M. R. Hudson, W. L. Queen, J. A. Mason, D. W. Fickel, R. F. Lobo, C. M. Brown, Unconventional, highly-selective $CO_2$ adsorption in zeolite SSZ-13. *J. Am. Chem. Soc.* **2012**, *134*, 1970-1973.

[36] J. Liu, N. He, W. Zhou, L. Lin, G. Liu, C. Liu, J.Wang, Q. Xin, G. Xiong, H. Guo, Isobutane aromatization over a complete Lewis acid Zn/HZSM-5 zeolite catalyst: performance and mechanism. *Catal. Sci. Technol*. **2018**, *8*, 4018-4029.

[37] J. Liu, N. He, W. Zhou, M. Shu, L. Lin, J. Wang, R. Si, G. Xiong, Q. Xin, H. Guo, Operando dual beam FTIR spectroscopy unravels the promotional effect of Zn on HZSM-5 in isobutane aromatization. *Catal. Sci. Technol*. **2019**, *9*, 1609-1620.

[38] S. M. T. Almutairi, B. Mezari, P. C. M. M. Magusin, E. A. Pidko, E. J. M. Hensen, Structure and reactivity of Zn-modified ZSM-5 zeolites: the importance of clustered cationic Zn complexes. *ACS Catal.* **2012**, *2*, 71-83.

[39] S. Brunauer, P. H. Emmett, E. Teller, *J. Am. Chem. Soc*. **1938**, *60*, 309-319.

[40] B. C. Lippens, J. H. Deboer, Studies on pore systems in catalysts: the V-t method. *J. Catal*. **1965**, 4, 319-323.

[41] M. Thommes, K. Kaneko, A. V. Neimark, J. P. Olivier, F. Rodriguez-Reinoso, J. Rouquerol, K. S. W. Sing, Physisorption of gases, with special reference to the evaluation of surface area and pore size distribution. *Pure Appl. Chem*. **2015**, *87*, 1051-1069.

[42] M. J. Frisch, G. W. Trucks, H. B. Schlegel, G. E. Scuseria, M. A. Robb, J. R. Cheeseman, G. Scalmani, V. Barone, B. Mennucci, G. A. Petersson, H. Nakatsuji, Gaussian 09, revision A.1. Gaussian, Inc.: Wallingford, CT, **2009**.

[43] V. P. Ananikov, D. G. Musaev, K. Morokuma, Real size of ligands, reactants and catalysts: Studies of structure, reactivity and selectivity by ONIOM and other hybrid computational approaches. *J. Mol. Catal. A* **2010**, *324*, 104-119.

[44] J.-D. Chai, M. Head-Gordon, Long-range corrected hybrid density functionals with damped atom-atom dispersion corrections. *Phys. Chem. Chem. Phys*. **2008**, *10*, 6615-6620.

[45] E. A. Pidko, R. A. van Santen, Activation of light alkanes over zinc species stabilized in ZSM-5 zeolite: a comprehensive DFT study. *J. Phys. Chem. C* **2007**, *111*, 2643-2655.

**Table 1.** $N_2$ physisorption data of Na-based zeolites with different pore structure type and Zn modified zeolites.

| Catalyst | Code | Si:Al[a] | $S_{BET}$[b] ($m^2 g^{-1}$) | $S_{micro}$[c] ($m^2 g^{-1}$) | $V_{pore}$ ($cm^3 g^{-1}$) | $V_{micro}$ ($cm^3 g^{-1}$) |
|---|---|---|---|---|---|---|
| NaSSZ-13 | NaS50 | 50 | 698 | 666 | 0.34 | 0.30 |
| $Zn_{0.89}$/NaSSZ-13 | $Zn_{0.89}$/NaS50 | 50 | 688 | 654 | 0.34 | 0.30 |
| $Zn_{1.70}$/NaSSZ-13 | $Zn_{1.70}$/NaS50 | 50 | 674 | 638 | 0.33 | 0.29 |
| $Zn_{2.92}$/NaSSZ-13 | $Zn_{2.92}$/NaS50 | 50 | 656 | 617 | 0.33 | 0.28 |
| NaZSM-5 | NaZ50 | 50 | 363 | 274 | 0.20 | 0.11 |
| $Zn_{0.72}$/NaZSM-5 | $Zn_{0.72}$/NaZ50 | 50 | 346 | 262 | 0.19 | 0.11 |
| $Zn_{1.90}$/NaZSM-5 | $Zn_{1.90}$/NaZ50 | 50 | 334 | 255 | 0.19 | 0.11 |
| $Zn_{2.50}$/NaZSM-5 | $Zn_{2.50}$/NaZ50 | 50 | 325 | 247 | 0.19 | 0.11 |
| NaMCM-22 | NaMCM | 28 | 512 | 388 | 0.54 | 0.16 |
| $Zn_{9.82}$/NaMCM-22 | $Zn_{9.82}$/NaMCM | 28 | 336 | 248 | 0.37 | 0.10 |
| NaY | NaY | 5 | 749 | 722 | 0.32 | 0.29 |
| $Zn_{7.29}$/NaY | $Zn_{7.29}$/NaY | 5 | 578 | 550 | 0.27 | 0.23 |
| NaSAPO-34 | NaSAPO | 0.2 | 530 | 524 | 0.25 | 0.21 |
| $Zn_{3.89}$/NaSAPO-34 | $Zn_{3.89}$/NaSAPO | 0.2 | 362 | 355 | 0.18 | 0.15 |

[a] XRF. [b] BET method applied to the $N_2$ isotherm. [C] *t*-Plot method applied to the $N_2$ isotherm.

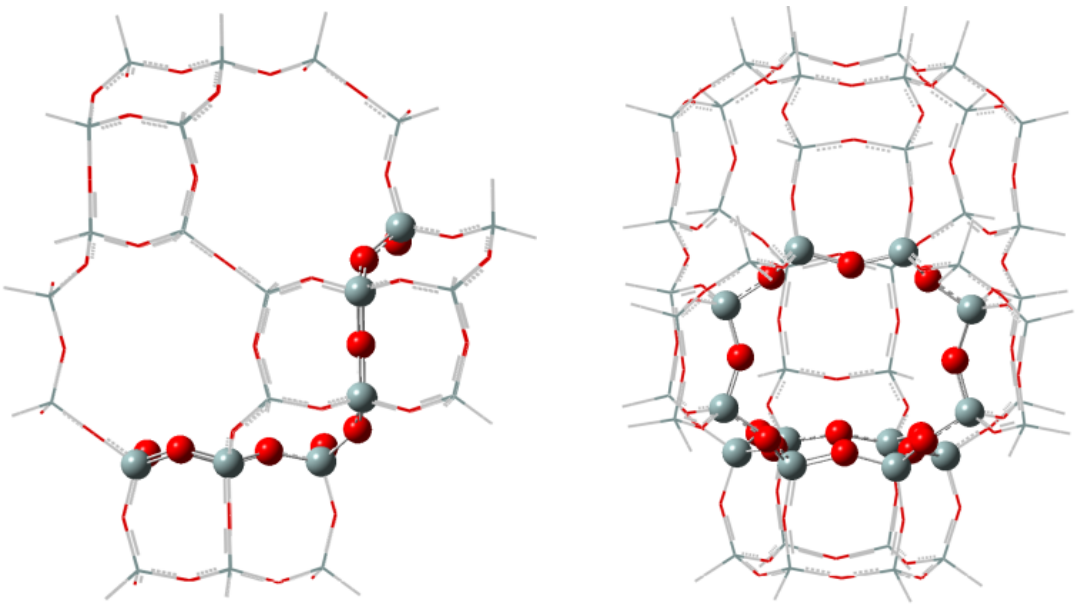

**Figure 1.** Side and top view of the 48T ONIOM cluster. The atoms treated with the ωB97XD and UFF functionals are depicted with ball and stick, and with wire frame, respectively.

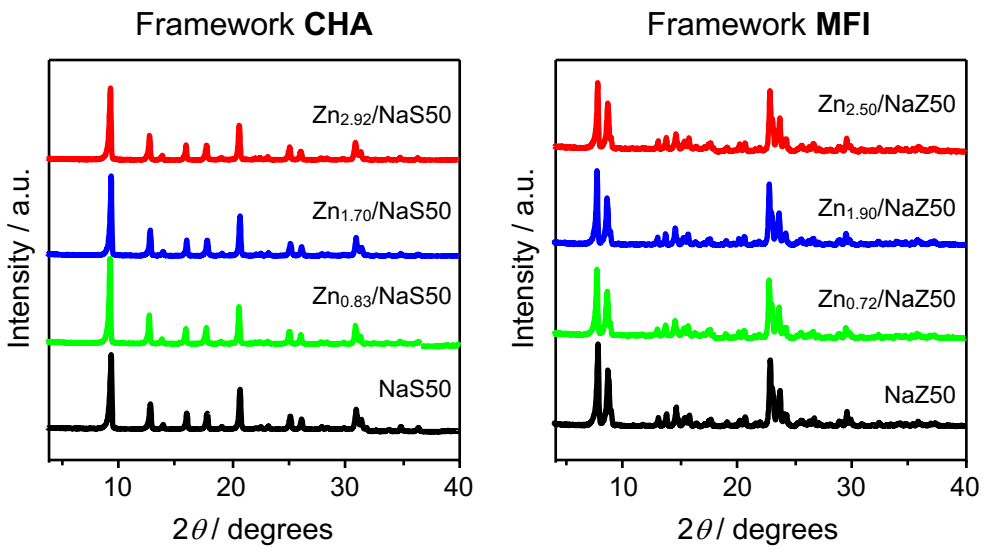


**Figure 2.** X-ray diffraction patterns of the different Zn-based zeolite catalysts.

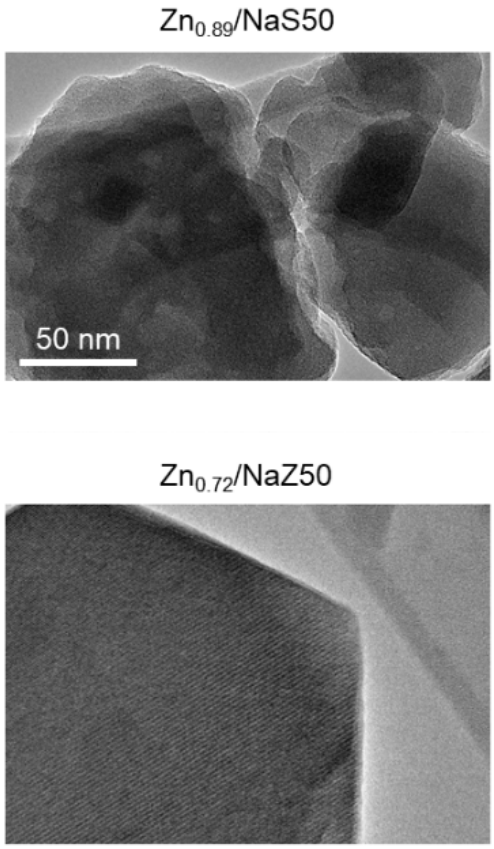


**Figure 3.** Transmission electron micrographs of different Zn-based zeolite catalysts.

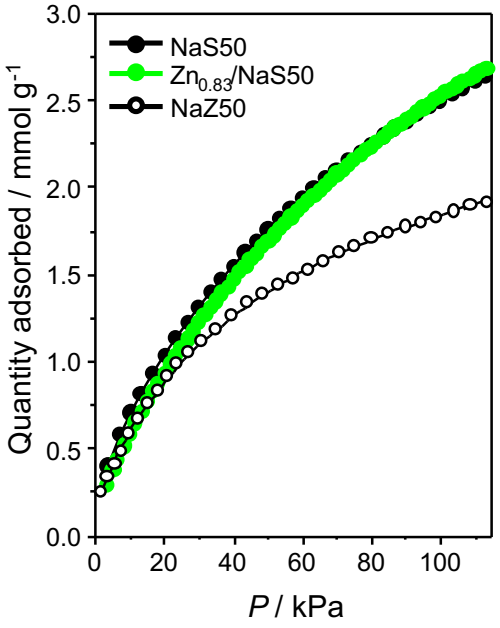


**Figure 4.** $CO_2$ physisorption data of NaS50 and $Zn_{0.89}$/NaS50 catalysts.

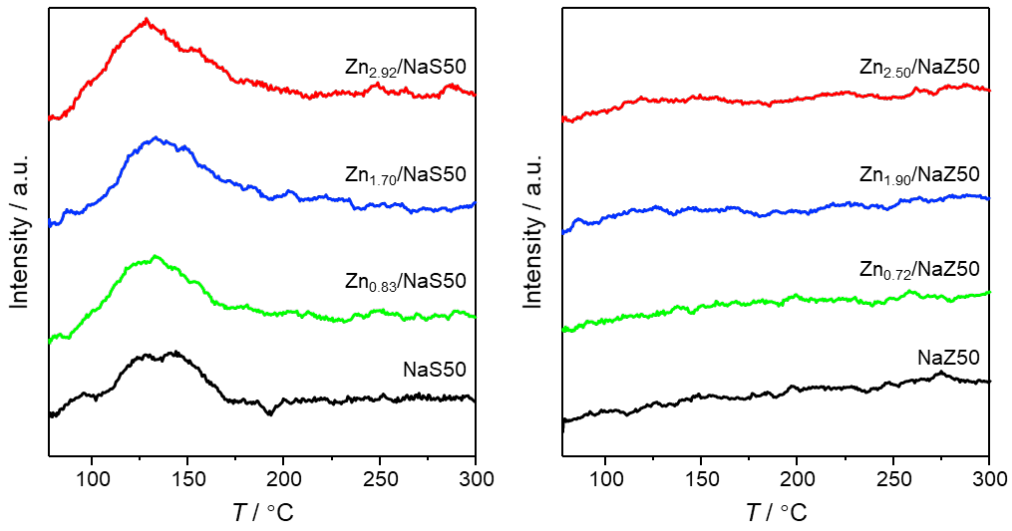


**Figure 5.** $CO_2$ temperature-programmed desorption of different Zn-based zeolite catalysts.

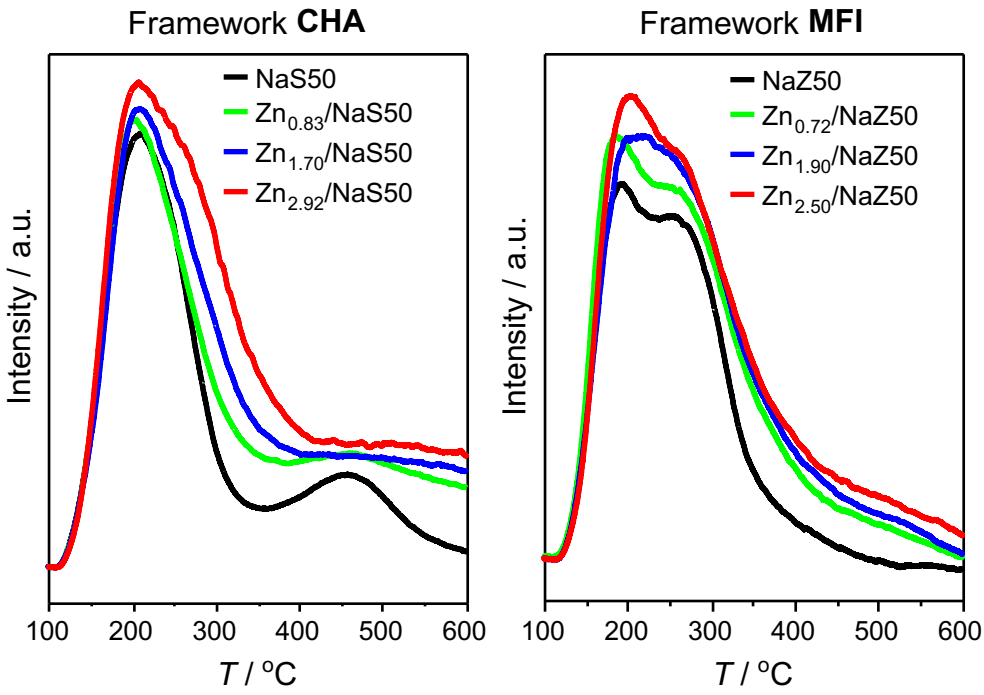


**Figure 6.** $NH_3$ temperature-programmed desorption of different Zn-based zeolite catalysts.

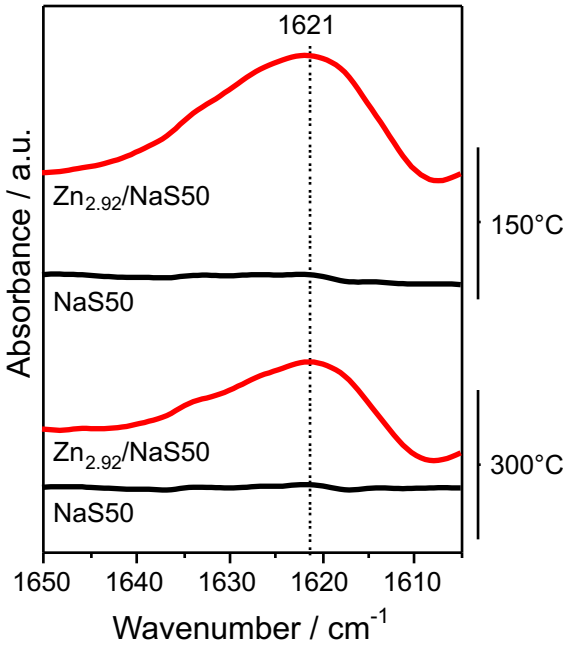


**Figure 7.** Fourier-transform infrared spectroscopy of NaS50 and $Zn_{2.92}$/NaS50 prior and after pyridine adsorption at different temperatures. The peak at 1621 $cm^{-1}$ points to the presence of Lewis acid sites as a result of the incorporation of Zn into the zeolite framework.

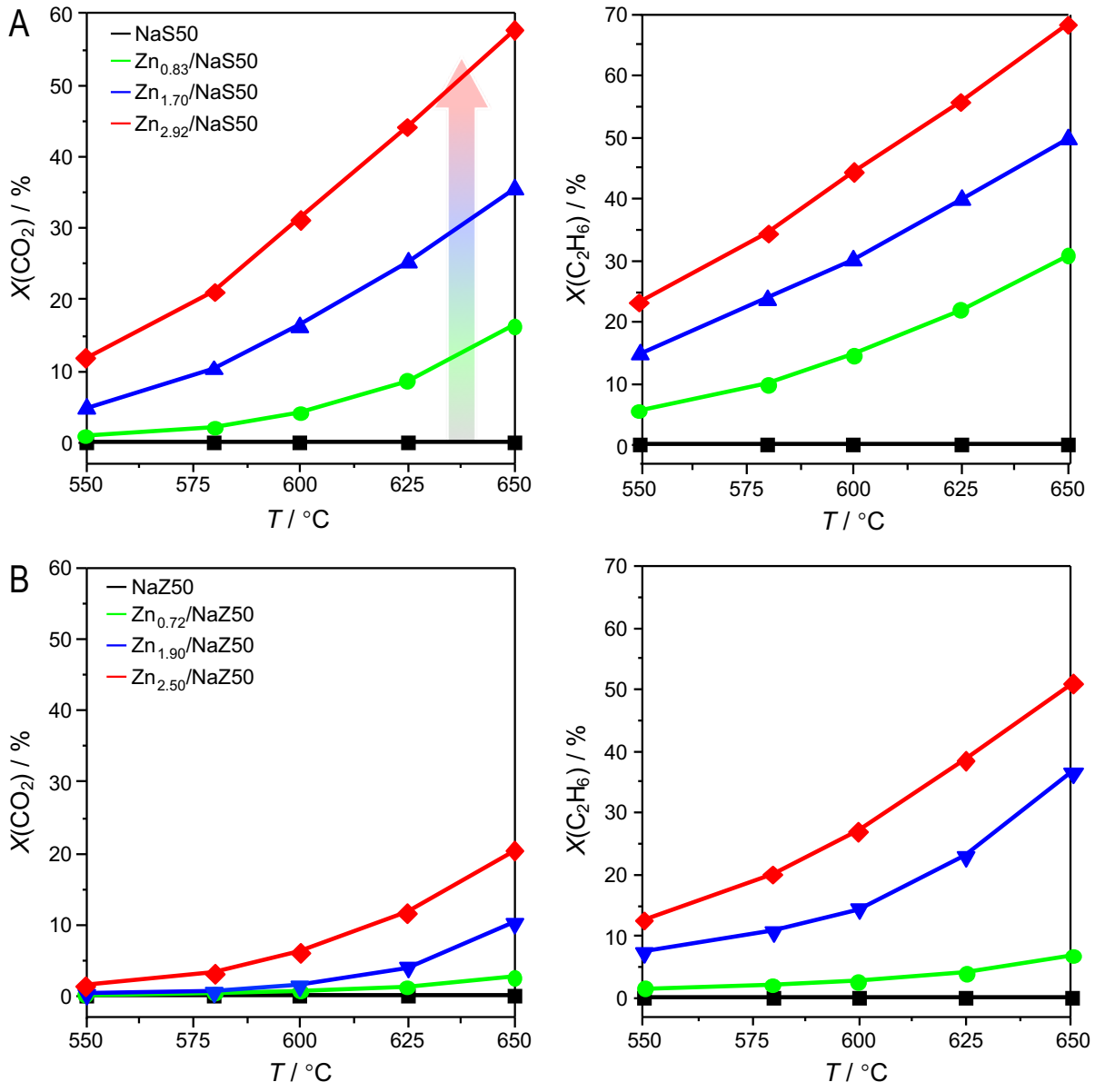


**Figure 8.** Influence of the Zn loadings on the conversion of $CO_2$ and $C_2H_6$ over different Zn-based NaS50 (a) and NaZ50 (b) zeolites. Conditions: temperature = 550-650°C, pressure = 0.1 MPa, $CO_2$:$C_2H_6$=1, and GHSV = 3600 mL $h^{-1}$ $g_{cat}^{-1}$.

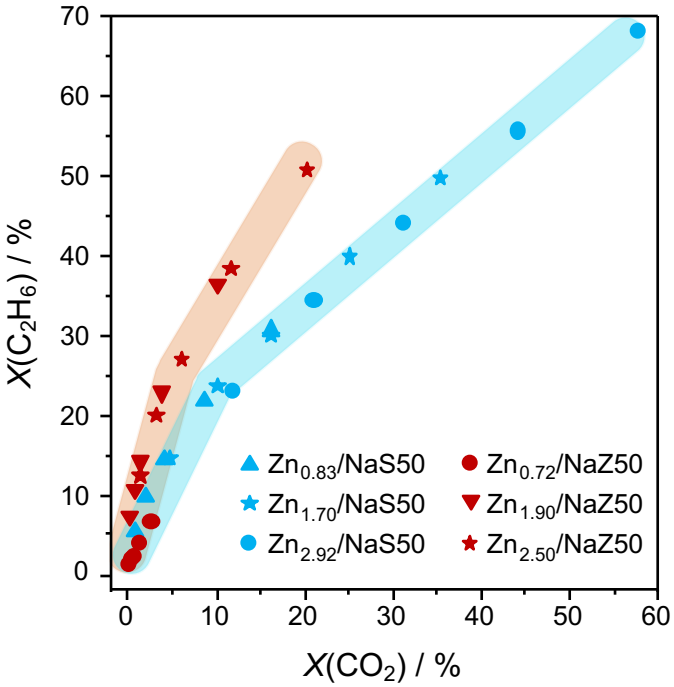


**Figure 9.** Conversion of $C_2H_6$ as a function of the conversion of $CO_2$ over different Zn-based NaS50 and NaZ50 zeolites. Conditions in Figure 8.

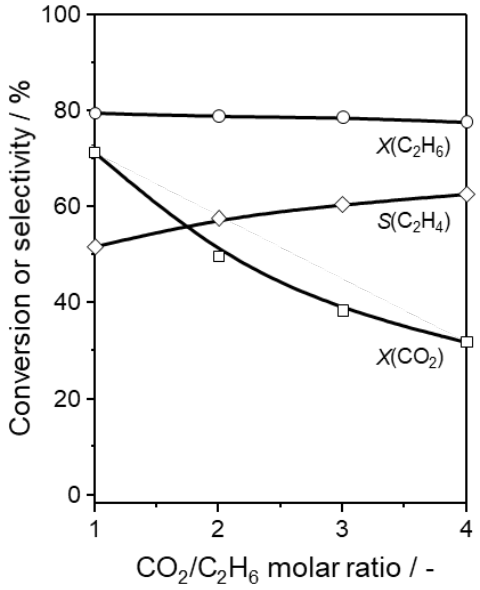


**Figure 10.** Influence of the $CO_2$:$C_2H_6$ molar ratio on catalytic performance of $Zn_{2.50}$/NaZ50 catalysts. Conditions: temperature = 650°C, pressure = 0.1 MPa, and GHSV = 3600 mL $h^{-1}$ $g_{cat}^{-1}$.

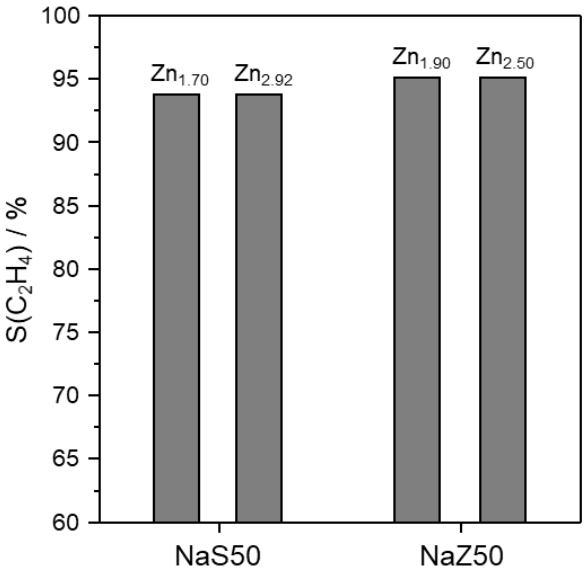


**Figure 11.** Selectivity to $C_2H_4$ over different Zn-based NaS50 catalysts, at a $CO_2$ conversion level of 10%. Conditions: temperature = 650°C, pressure = 0.1 MPa, $CO_2$:$C_2H_6$=1, and GHSV = 3600 mL $h^{-1}$ $g_{cat}^{-1}$.

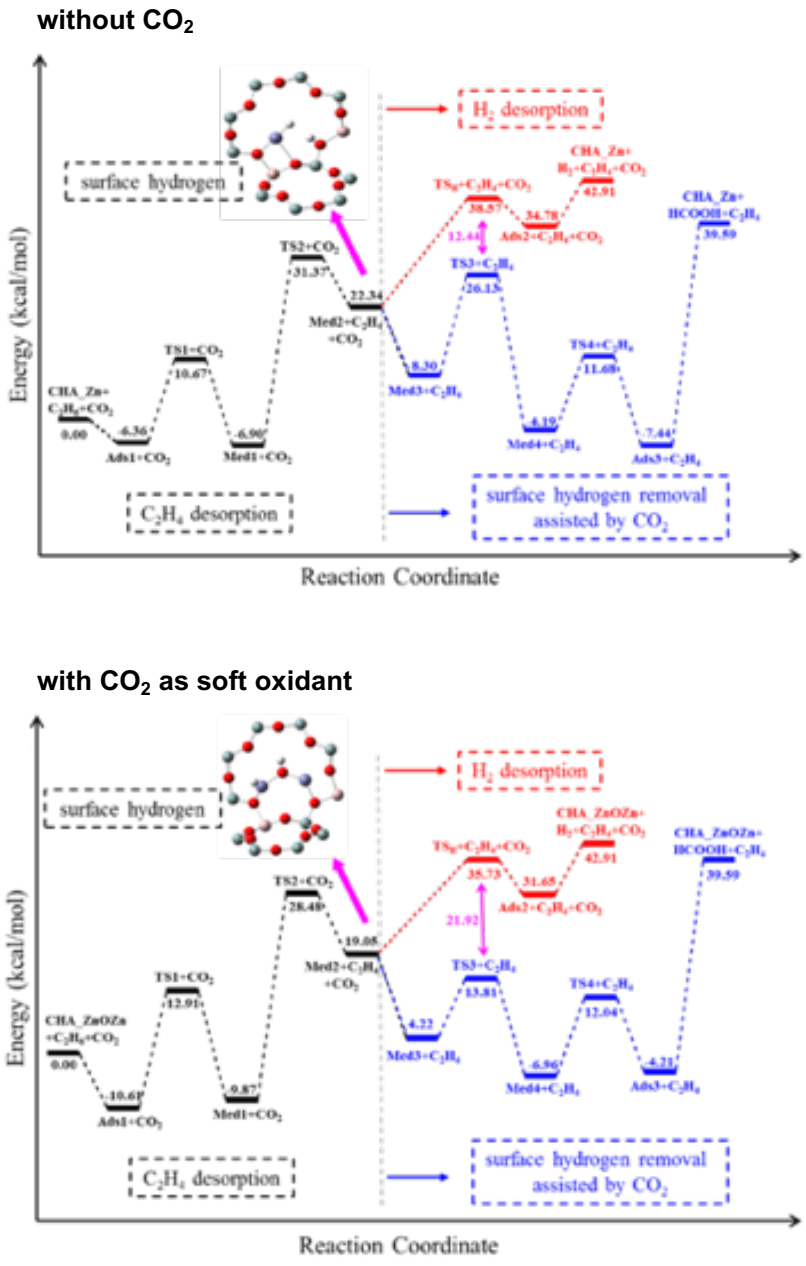


**Figure 12.** Energy profiles for the conversion of ethane on $Zn^{2+}$, without (a) and with (b) $CO_2$ as soft oxidant.

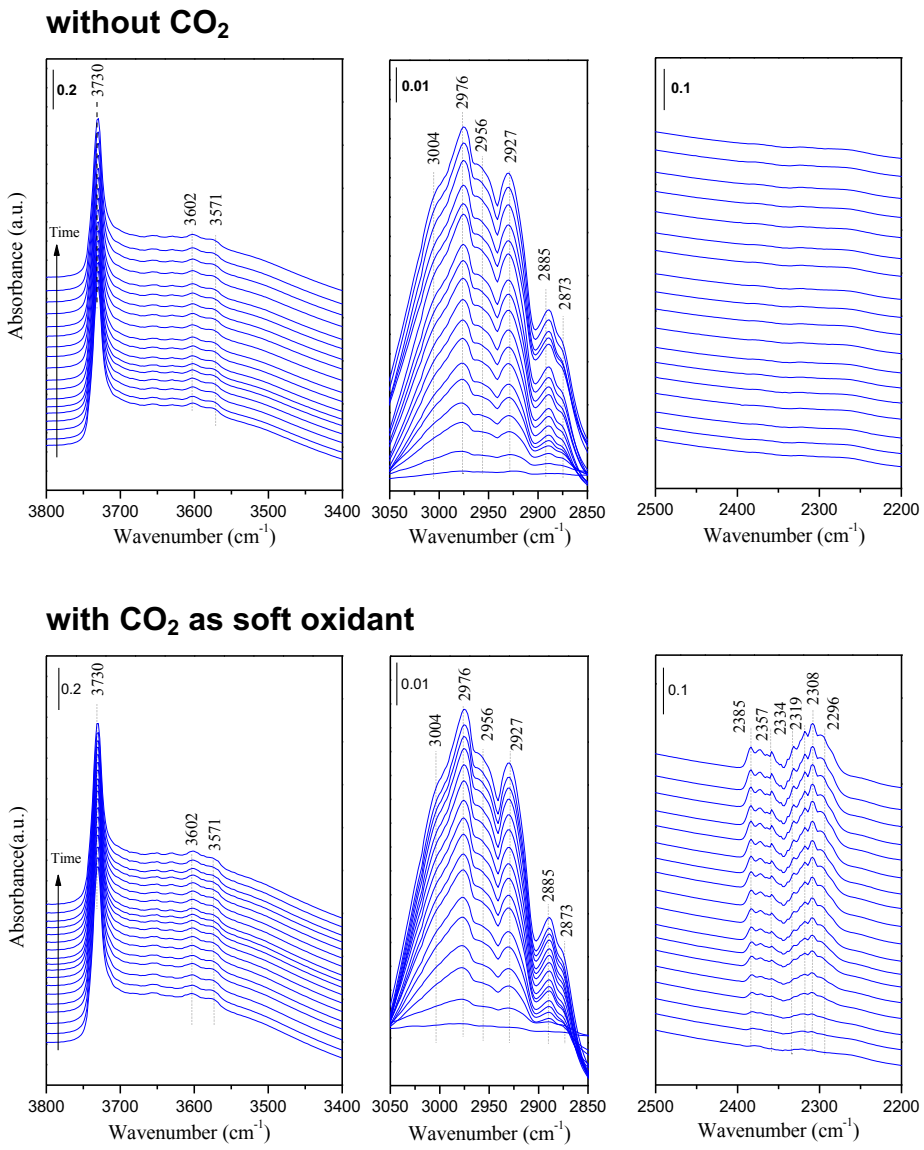


**Figure 13.** Selected spectra of ethane conversion over $Zn_{2.92}$/NaS50 at 300°C, 0.1 MPa, and GHSV = 3600 mL $h^{-1}$ $g_{cat}^{-1}$ obtained using a DB-FTIR in a flowing mixture of ethane and helium gas (2% ethane in helium) for 50 minutes, without (a) and with (b) $CO_2$ as soft oxidant ($CO2:C_2H_6$ = 1).

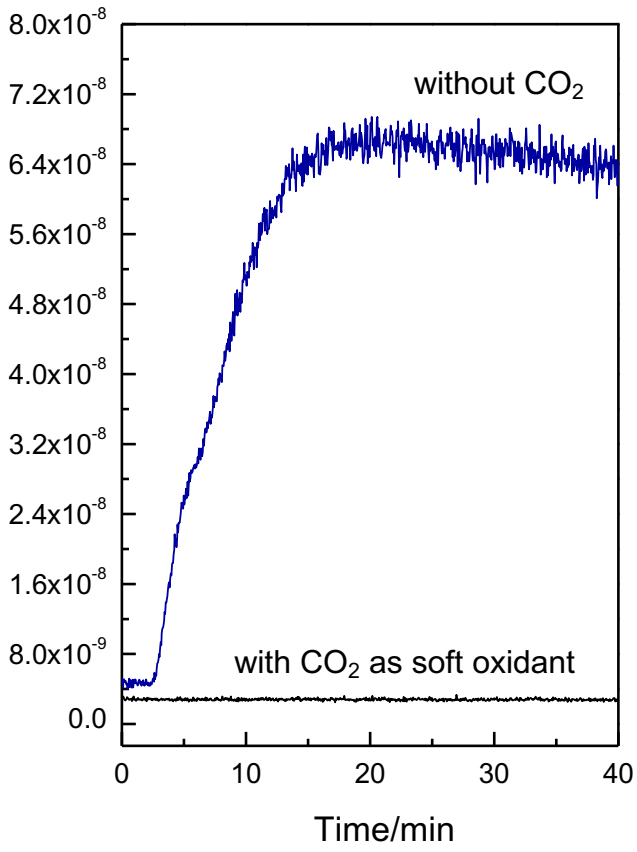


**Figure 14.** Mass spectra from the DB-FTIR effluent without (black line) and with (blue line) CO2 as a soft oxidant. Conditions in Figure 13.